Electronic structure and angular momentum coupling as reflected in electron excitation out of rare-gas metastable levels: Excitation cross sections of krypton

R. O. Jung, Tom E. Stone, John B. Boffard, L. W. Anderson, and Chun C. Lin
Department of Physics, University of Wisconsin, Madison, Wisconsin 53706, USA
(Received 6 December 2005; published 27 February 2006)

We present measurements of electron-impact excitation cross sections into levels of the $4p^5 5p$ configuration from the $J=0$ and $J=2$ metastable levels of krypton. Metastable-atom targets were generated using two different sources, a hollow-cathode discharge and via charge-exchange collisions between a fast Kr^+ beam and Cs atoms. The metastable atoms are excited to $4p^5 5p$ levels by a monoenergetic electron beam and the fluorescence from the levels are used to determine the excitation cross sections. Laser quenching of the hollow-cathode target is used to separate the signal contributions from excitation of the two metastable levels. Like excitation from the metastable levels of Ar, cross sections for dipole-allowed excitations are generally larger than ones for dipole-forbidden excitations. Krypton differs from Ar and Ne, however, in having a larger spin-orbit coupling for the $4p^5$ core so that the energy levels of each excited configuration segregate into two tiers based on the value of the core angular momentum. Cross sections for dipole-allowed excitation with a change in the core angular momentum are not only much smaller than their core-preserving counterparts, but also have different energy dependence. The measured cross sections are compared with recent theoretical calculations and with previous experimental work.

DOI: 10.1103/PhysRevA.73.022722 PACS number(s): 34.80.My, 34.80.Dp, 52.20.Fs

I. INTRODUCTION

One aim of studying electron-impact excitation cross sections is to develop both a qualitative and a quantitative understanding of the link between atomic structure and collision dynamics. For example, excitation processes that correspond to optically allowed transitions generally have larger electron excitation cross sections than optically forbidden transitions. Furthermore, the magnitude of the excitation cross section is closely related to the optical oscillator strength of the transition. A second example for *LS*-coupled atomic levels is that the cross sections for an $n^{2S+1}L_J$ series share the same energy dependence, with the only real difference being an n dependent scaling parameter for the magnitude. An area of interest lies in examples where these general principles seem to falter, since they point to interesting aspects of collision dynamics. One example where these conceptual rules lead one astray is electron impact excitation into the Na(nP) levels. The energy dependence of the Na($3S \rightarrow 3P$) excitation cross section, a broad peak at low energies, differs markedly from the Na($3S \rightarrow nP, n \geqslant 4$) excitation cross sections which have an additional feature of a sharp peak at low energies [1].

The excitation of metastable atoms provides a test for developing a deeper understanding of these types of collision dynamics. Previous experiments by our research group on the electron excitation from the metastable levels of Ne [2] and Ar [3,4] have confirmed that in these cases the cross sections for dipole-allowed excitations are indeed very large, with magnitudes that scale with optical oscillator strength of the corresponding optical transition from the metastable level, while dipole-forbidden excitations have smaller cross sections with a distinctly different energy dependence. In the case of Ar, for example, the two metastable levels of the $3p^5 4s$ electronic configuration have a total angular momentum of $J=0$ (the $1s_3$ level in Paschen's notation) or $J=2$ ($1s_5$ level). Excitation of the metastable atoms into the levels of the $3p^5 4p$ configuration satisfy the optical dipole selection rule $\Delta l=1$. Among the levels of the $3p^5 4p$, excitation out of the $J=2$ $1s_5$ metastable level favors those final levels with $J=1,2,3$, whereas excitation out of the $J=0$ $1s_3$ level favors only the $J=1$ levels in accordance with the dipole selection rule $\Delta J=0, \pm 1$ and $J=0 \not\rightarrow J=0$. Excitation from both the $1s_3$ and $1s_5$ levels into the $J=0$ levels of the $3p^5 4p$ configuration violate the optical dipole selection rules and are indeed found to have smaller cross sections [4].

For excitation from the metastable levels of Kr, the situation is more complicated. The experimental measurements by Mityureva, Penkin, and Smirnov [5] are consistent with the scaling relationship between cross-section magnitude and oscillator strength. Our preliminary measurements [6,7] as well as theoretical calculations of Dasgupta *et al.* [8] find that the cross sections are also influenced by another factor that is related to the coupling of the individual angular momentum vectors within the atom to form the total angular momentum J. An excited Kr atom consists of the $4p^5$ ion core (with orbital and spin angular momentum $l_c=1$ and $s_c=1/2$, respectively) plus an outer electron nl (with orbital and spin angular momenta l_o and s_o). The Kr($4p^5$) ion core has a large spin-orbit coupling resulting in two levels, $^2P_{3/2}$ and $^2P_{1/2}$, separated by 0.6 eV. For the Kr($4p^5 5s$) configuration the $^2P_{3/2}$ ion core couples to a $5s$ electron to form the $J=2$ $1s_5$ metastable level and the $J=1$ $1s_4$ resonance level; and the $^2P_{1/2}$ ion core couples to a $5s$ electron to form the $J=1$ $1s_2$ resonance level and the $J=0$ $1s_3$ metastable level. Collectively we refer to any level with $^2P_{1/2}$ parentage as having a "core angular momentum" $j_c=1/2$, and similarly $j_c=3/2$ for $^2P_{3/2}$ parentage. Figure 1 shows that the 0.6-eV splitting of the ion core levels is retained in $4p^5 5s$ atomic levels, with an upper tier of the two $j_c=1/2$ levels and a

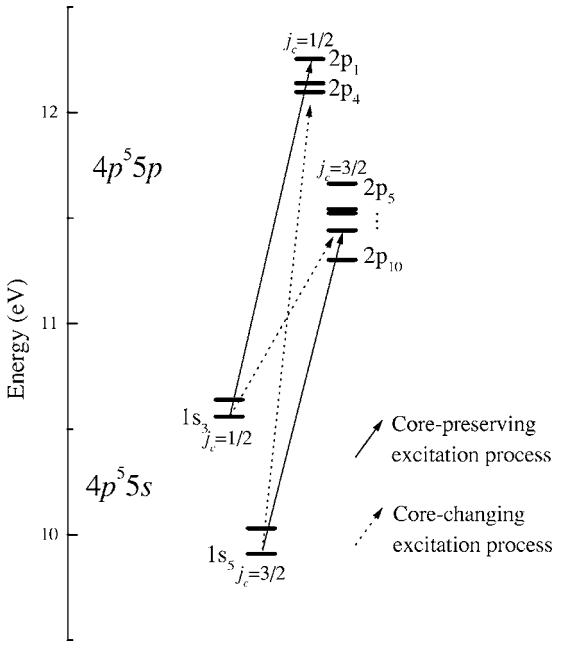

FIG. 1. Energy levels of the $4p^5 5s$ and $4p^5 5p$ configurations of krypton.

lower tier of the two $j_c=3/2$ levels. Likewise, the ten levels of the $4p^5 5p$ configuration (referred to as the $2p_1$ to $2p_{10}$ in Paschen's notation) split into two tiers based on j_c. In Table I we provide additional information for the levels of interest.

To the extent that the core angular momentum j_c is a good quantum number, excitation from the $1s_5$ metastable level ($j_c=3/2$) into one of the upper tier $2p_1-2p_4$ levels ($j_c=1/2$) requires a single collision both to excite the outer electron and excite the core. These core-changing excitation cross sections have been found to be generally much smaller than core-preserving excitation cross sections [7]. Unlike the total angular momentum J, the core angular momentum j_c is, at best, approximately a good quantum number. An eigenstate of the $4p^5 5p$ (or $4p^5 5s$) configuration can be decomposed into a $|j_c=3/2\rangle$ component and a $|j_c=1/2\rangle$ component. Only when one component greatly exceeds the other is j_c an approximately good quantum number. It is then useful to speak of "core-preserving" and "core-changing" collisions and we will refer to the dominance of the former over the latter as core propensity. In contrast, the smaller spin-orbit splitting of the $^2P_{1/2}$ and $^2P_{3/2}$ levels in Ne and Ar (0.10 and 0.17 eV, respectively) are overwhelmed by the coupling of the outer valence electron with the ion core, leading to a scheme usually referred to as "intermediate coupling" where j_c is not such a good descriptor.

TABLE I. Paschen and Racah notations for the Kr energy levels used in this work. E is the energy of the level relative to the ground state.

Paschen	J	j_c	Racah	E (eV)
$2p_1$	0	1/2	$5p'[\frac{1}{2}]_0$	12.26
$2p_2$	2	1/2	$5p'[\frac{3}{2}]_2$	12.14
$2p_3$	1	1/2	$5p'[\frac{1}{2}]_1$	12.14
$2p_4$	1	1/2	$5p'[\frac{3}{2}]_1$	12.10
$2p_5$	0	3/2	$5p[\frac{1}{2}]_0$	11.67
$2p_6$	2	3/2	$5p[\frac{3}{2}]_2$	11.55
$2p_7$	1	3/2	$5p[\frac{3}{2}]_1$	11.53
$2p_8$	2	3/2	$5p[\frac{5}{2}]_2$	11.44
$2p_9$	3	3/2	$5p[\frac{5}{2}]_3$	11.44
$2p_{10}$	1	3/2	$5p[\frac{1}{2}]_1$	11.30
$1s_2$	1	1/2	$5s'[\frac{1}{2}]^o_1$	10.64
$1s_3$	0	1/2	$5s'[\frac{1}{2}]^o_0$	10.56
$1s_4$	1	3/2	$5s[\frac{3}{2}]^o_1$	10.03
$1s_5$	2	3/2	$5s[\frac{3}{2}]^o_2$	9.91

Measuring electron-impact excitation cross sections out of the two metastable levels of Kr into all ten levels of the $4p^5 5p$ configuration could in principle allow 20 cross sections to be determined for various types of collision processes: (i) core-preserving and core-changing excitations, (ii) dipole-allowed and dipole-forbidden excitations, and (iii) excitations with a wide range of oscillator strengths. In this paper we report on the trends observed in a systematic survey of this system, including measurements of 13 of the 20 possible cross sections. In the following section we describe the experimental methods used to measure the cross sections including our calibration methods (Secs. II A 3 and II B 3) and how we separate the contributions from the two different initial states (Sec. II B 2). In Sec. III we present our measurements and in Sec. IV discuss the results and compare them with previous experimental and theoretical works.

II. EXPERIMENTAL METHOD

Two different experimental apparatuses were used to obtain the cross sections reported here. The first apparatus creates metastable krypton atoms via charge exchange between a fast ion beam and a cesium vapor target (Sec. II A). This source is used to measure cross sections out of the $1s_5$ metastable level at high electron energies (>10 eV), and for absolute measurements. The second source creates a much larger metastable number density using a hollow cathode discharge as the source of metastable atoms (Sec. II B). This source is used for relative measurements of cross sections from both the $1s_3$ and $1s_5$ metastable levels at low electron energies.

A. Fast beam target

1. Description

Since a general exposition of the apparatus has already been provided in Ref. [9], only a brief description pertaining to the present experiment is provided here. A 2.5-keV Kr ion beam is produced by an rf ion source. The ion beam is passed through a recirculating Cs vapor target. Near resonant charge exchange between Kr^+ and Cs atoms converts a sub-

stantial portion of the ion beam into a fast neutral beam (cf. Sec. II A 2). After the remaining ions are removed from the beam with a set of deflection plates, the neutral beam is crossed at right angles by a monoenergetic electron beam. Atoms excited to $4p^5 5p$ levels are detected by monitoring the fluorescence from their decay. The optical system, located at right angles to both the electron and atom beams, consists of a photomultiplier tube (PMT) operating in photon-counting mode along with a narrow-band interference filter (0.3–0.5 nm full width at half maximum) used to provide spectral isolation of a single emission line. Since excited atoms in the fast beam travel some distance before they decay, the distance between the electron gun and optical viewing region can be varied by translating the electron beam. The fast beam is monitored by a detector that can be operated as (i) a Faraday cup for ions, (ii) a secondary electron detector for neutrals, or (iii) a thermal detector for neutrals or ions. Double modulation of the electron and neutral beams is used to extract the metastable excitation signal.

2. Target composition

As stated previously, metastable atoms are formed via the charge exchange reaction

$$\mathrm{Kr}^+(4p^5) + \mathrm{Cs} \rightarrow \mathrm{Kr}(4p^5 5s) + \mathrm{Cs}^+ + \Delta E, \tag{1}$$

where ΔE is the energy defect between the initial and final states. In the simplest approximation, if we assume the $4p^5 5s$ levels are populated according to their statistical weights, we would find the neutral beam to be composed of atoms in the $1s_2 : 1s_3 : 1s_4 : 1s_5$ levels in the ratio 3:1:3:5. Atoms created in the $1s_2$ and $1s_4$ resonance levels decay to the ground state before they reach the collision region. Since the excitation cross sections out of the ground state are substantially smaller than the metastable excitation cross sections, this ground-state fraction in the target does not contribute significantly to the measured signal rate.

Since the calibration of the $1s_5 \rightarrow 2p_9$ excitation cross section is directly dependent on the fraction of $1s_5$ atoms in the fast beam, a slightly more detailed analysis of the beam composition is warranted. We do not directly measure the $1s_5$ fraction, but calculate it based on charge exchange cross sections. In addition to charge exchange into the $4p^5 5s$ levels, two additional channels also contribute to the composition of the neutral beam. Nonresonant charge transfer into $4p^5 5p$ levels followed by decay to $4p^5 5s$ levels slightly enhances the $1s_5$ fraction, while resonant charge exchange between the ion beam and residual Kr gas in the vacuum system increases the ground-state fraction. Including these factors along with the cross section results of Ref. [10] for charge exchange directly into the $4p^5 5s$ levels, we estimate the $1s_5$ fraction of the fast beam to be 0.42 ± 0.08. Considering the small size of core-changing cross sections [7], the fraction of atoms in the $1s_3$ metastable level is too small (≤ 0.06) to contribute significantly to the measured signal rates for excitation into the $2p_6$ and $2p_9$ levels.

3. Absolute calibration

The electron-impact excitation signal rate S at some fixed energy is equal to

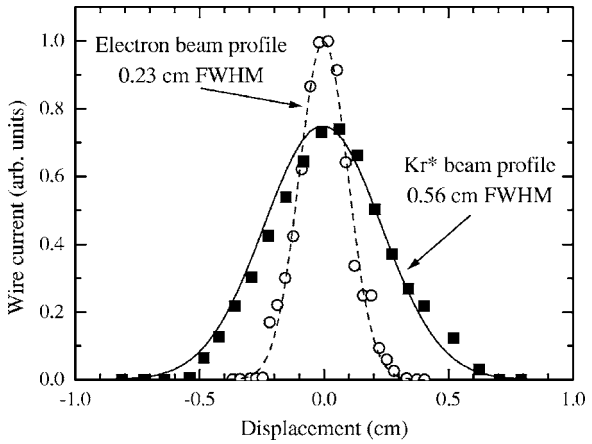

FIG. 2. Spatial profiles of the electron beam (at an energy of 100 eV) and the metastable krypton beam.

$$S = \xi Q \int \Omega(\vec{r}) n(\vec{r}) \frac{J_e(\vec{r})}{e} d\vec{r}, \tag{2}$$

where ξ is the total (optics and electronics) detector sensitivity, Q is the desired emission cross section, $\Omega(\vec{r})$ is the probability of detecting an atom excited at position $\vec{r}$, $n(\vec{r})$ is the target density at $\vec{r}$, $J_e(\vec{r})$ is the current density of the electron beam, and e is the magnitude of the elementary charge. To determine ξ for our experimental apparatus we take the ratio of two signal rates: one with the metastable fast beam target S_m and one obtained by filling the chamber with Kr gas, S_{gs}. In the latter case the signal rate is proportional to the emission cross section from the ground state of Kr which has been previously measured [11]. The functional forms of both $\Omega(\vec{r})$ and $n(\vec{r})$ differ for the two targets. In the case of the ground-state target, the target number density is spatially uniform. The thermal velocity atoms also do not move very far in the time between when they are excited by the electron beam and when they decay. In contrast, the metastable target is not spatially uniform, but has a cylindrical symmetry. The high velocity of atoms in the fast beam also shifts the spatial distribution of decaying atoms downstream from the electron excitation region.

To determine the overlap integrals for the two cases we measure the spatial profiles of electron beam, metastable beam, and the size of the optical viewing region. Our coordinate system is defined such that the metastable beam propagates along the x axis, the electron beam along the y axis, and the optical system is oriented along the z axis. To obtain the beam profiles, we replace the detection optics with a rotating thin wire [9]. For the electron beam, we directly measure the electron beam current hitting the wire, whereas for the neutral beam the wire current is the result of secondary electron emission. Sample profiles are shown in Fig. 2. The wire measures the current density integrated along the length of the wire; thus for the electron beam we obtain the $j_e(y)$ electron-beam profile. Since this profile is essentially Gaussian, we assume $J_e(\vec{r})$ is cylindrically symmetric and can be written as $J_e(\vec{r}) = J_e^0 j_e(x) j_e(y)$ where J_e^0 carries the

magnitude of the beam profile and $j_e(x)$ and $j_e(y)$ are normalized spatial profiles.

The $1s_5$ metastable number density can be written as

$$n_m(\vec{r}) = f_m I_N j_m(y) j_m(z)/v_f, \tag{3}$$

where f_m is the fraction of $1s_5$ metastable atoms in the neutral beam, v_f the velocity of atoms in the fast beam (set by the ion-beam energy), and $j_m(y)$ and $j_m(z)$ are line-integrated profile functions normalized such that I_N is the neutral particle "current" (particles/s). The neutral particle current is obtained by comparing the thermal energy deposited in the neutral detector from the 2.5-keV fast neutral beam and a 2.5-keV ion beam for which we can easily measure the current.

Combining all the profile functions and other factors for the two cases of the fast metastable beam target and static ground-state gas target, we obtain (after some simplifications) the metastable excitation cross section in terms of the known ground-state excitation cross section,

$$Q_m = Q_{gs} \frac{S_m}{S_{gs}} \frac{v_f n_{gs}}{f_m I_N} \frac{\Phi_s}{\Phi_f} \frac{\int \Omega(y) dy}{\int j_m(y) \Omega(y) dy} \frac{\int j_e(z) dz}{\int j_e(z) j_m(z) dz}, \tag{4}$$

where Φ_s and Φ_f correspond to the x integrals,

$$\frac{\Phi_s}{\Phi_f} = \frac{\int j_e(x) \Omega(x) dx}{\int j_e(x) \Omega_f(x) dx}. \tag{5}$$

For the ground-state gas target, the probability of detecting an atom excited at x, $\Omega(x)$, is the same as the profile of the optical system obtained by translating an LED across the viewing region. For an excited atom in the fast beam target, $\Omega_f(x) = \Omega(x + v_f T)$, where T is the time between when the atom is excited and when it decays. We calculate the denominator of Eq. (5) using a model that includes the velocity of the atoms in the fast beam and the lifetime of the level of interest [12]. We can test the quality of this part of the calculation by experimentally varying the distance between the electron beam and the center of the optical viewing region by translating the electron gun as illustrated by Fig. 3.

For the $2p_9$ level at an electron energy of 100 eV we find $Q_m/Q_{gs} = 1130 \pm 290$, where the uncertainty includes both the statistical uncertainties and all of the systematic uncertainties such as the pressure (measured using a spinning rotor gauge), beam profiles, and estimation of f_m. To minimize the distortion to the electron-beam profile, we conduct the ground-state measurements at very low gas pressures (typically 2×10^{-7} Torr). Chilton *et al.* [11] have measured the ground-state apparent excitation cross section to be $(19 \pm 3) \times 10^{-19}$ cm^2 at 100 eV and a target pressure of 2 mTorr. Due to resonance radiation trapping of cascading levels, Chilton *et al.* found that the apparent cross section (which includes the cascade contribution from these resonance levels) increases with the target gas pressure [13]. Extrapolating to zero pressure we obtain a value of $(14 \pm 3) \times 10^{-19}$ cm^2. Tsurubuchi *et al.* [14] measured a significantly higher value of $(32 \pm 9.7) \times 10^{-19}$ cm^2 at 100 eV which was measured at a pressure below 5×10^{-5} Torr. Furthermore, they found that the $2p_9$ apparent cross section decreases with increasing pressure which they possibly attribute to radiation trapping of the 811.3-nm $1s_5$-$2p_9$ transition due to an increase in the number of $1s_5$ metastable atoms [14]. We resolved this difference in favor of the Chilton *et al.* value by measuring the 811.3-nm Kr emission cross section (at a pressure of 3×10^{-7} Torr) using for calibration the nearby 811.5-nm $1s_5$-$2p_9$ transition of Ar, for which the measurements of Chilton *et al.* [15] and Tsurubuchi *et al.* [16] are in good agreement. Multiplying our measured Q_m/Q_{gs} ratio by the Chilton *et al.* ground-state excitation cross section and including the added uncertainty in the ground-state cross section we find $Q_m(100 \text{ eV}) = (16 \pm 5) \times 10^{-16}$ cm^2. From the measured dependence of the excitation cross section with electron energy we find that $Q_m(5 \text{ eV}) = (52 \pm 18) \times 10^{-16}$ cm^2.

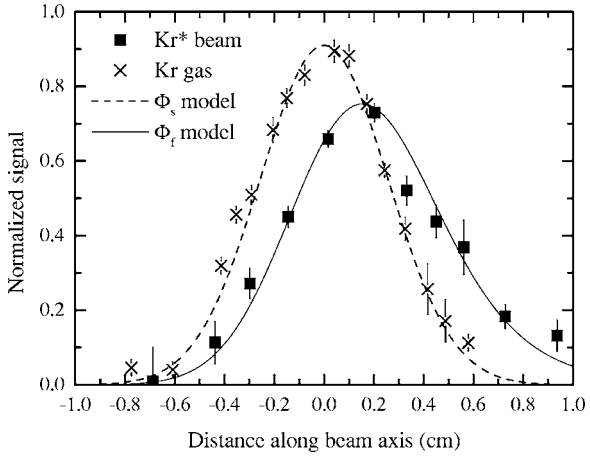

FIG. 3. Spatial variation of the $2p_9$ excitation signal at 50 eV as a function of the distance between the electron gun and center of the optical viewing region. For the static gas target, this is the convolution of the electron beam width and width of the viewing region. For the 2.5-keV fast beam target, the profile is shifted due to the motion of the atoms in the fast beam target between the point where they are excited by the electron beam and where they decay.

B. Hollow cathode discharge target

1. Description

The hollow cathode source is the same as that described in our previous work on excitation of metastable helium [17] and metastable argon [4] so only a brief description is offered here. The metastable Kr atoms are produced in a hollow cathode discharge. A 1-mm-diameter hole in the base of the hollow cathode allows atoms in both metastable levels and the ground level to enter a collision region where the atomic beam is crossed at right angles by an electron beam. Fluorescence from a particular $4p^5 5p$ level of interest is selected using a narrow bandwidth interference filter and is detected using a photomultiplier tube. The optical detection axis is oriented at right angles to the atomic beam and at 60° relative to the electron beam. This angle is very close to the

"magic angle" of 54.7° where the emission intensity is independent of polarization effects. As with the fast beam experiment, photon counting is used to extract the metastable excitation signal.

2. Target composition

The atoms flowing out of the hollow cathode discharge form a target containing atoms in both metastable levels and a large number of ground-state atoms. At electron energies below the threshold for excitation from the ground state ($\leqslant$10 eV), the emission signal is solely due to excitation from atoms in $4p^5 5s$ levels. Due to radiation trapping, we also allow for the possibility that the target may contain some $1s_2$ and $1s_4$ resonance levels in addition to atoms in the $1s_3$ and $1s_5$ metastable levels. Excited atoms exiting the discharge in all other levels will decay before they reach the collision region.

The relative number of atoms in $1s_2 : 1s_3 : 1s_4 : 1s_5$ levels in the unaltered target are measured by laser-induced-fluorescence (LIF). An Ar-ion pumped, single-mode, ring Ti:sapphire laser is used to create a low power ($\sim 10^{-5}$ W) laser beam that passes through the collision region in the same plane as the electron beam and collection optics axis. Fluorescence from the decay of atoms pumped into a $2p_x$ level is detected with the same optical system used for the collection of electron excitation signal. Analogously to Eq. (2), this signal is equal to

$$S^{\mathrm{LIF}} = \Gamma \xi \int \sigma(\nu)(\nu - \nu_0) d\nu \int \Omega(\vec{r}) n(\vec{r}) \frac{I(\vec{r})}{h\nu} d\vec{r}, \qquad (6)$$

where Γ is the branching fraction of the observed fluorescence transition observed, I is the intensity of the laser of frequency ν, h is Plank's constant, and σ is the photon absorption cross section. Note that the signal is integrated as we slowly swept the laser 10 GHz around the pump transition. This allows us to use the standard relation between σ and the oscillator strength f of the pump transition,

$$\int \sigma(\nu)(\nu - \nu_0) d\nu = \pi r_0 c f, \qquad (7)$$

where c is the speed of light and r_0 is the classical radius of the electron. To measure the $1s_5 : 1s_3$ number density ratio, we pump the $1s_5 \rightarrow 2p_9$ transition at 811.3 nm and observe the fluorescence emissions at the same wavelength; and then tune the laser to the 805.9-nm $1s_3 \rightarrow 2p_4$ transition and observe the fluorescence from the same 805.9-nm emission line. Assuming that the spatial distributions of the metastable atoms and laser beams are the same in the two cases, the number density ratio can be found from

$$\frac{n_5}{n_3} = \frac{S_5^{\mathrm{LIF}}}{S_3^{\mathrm{LIF}}} \frac{\Gamma_3}{\Gamma_5} \frac{f_3}{f_5} \frac{P_3}{P_5} \frac{\lambda_3}{\lambda_5} \left(\frac{\xi_3}{\xi_5} \right), \qquad (8)$$

where P is the recorded laser power, and the subscripts 5 and 3 refer, respectively, to the cases with the laser tuned to the transition out of the $1s_5$ and $1s_3$ levels. The unknown wavelength dependent sensitivities, ξ's, at the two observed wavelengths are eliminated by calibrating the PMT signal with a known signal rate at the same wavelength. We have used two different sources both of which yielded the same results: (i) the ground-state electron-impact excitation signal using the known ground-state excitation cross sections [11], and (ii) the signal from a Kr capillary discharge lamp that was separately calibrated at each emission wavelength (cf. Sec. II B 3).

We find the $1s_5 : 1s_3$ ratio to be $(12 \pm 2) : 1$. This is substantially above the 5:1 ratio based solely on statistical weights. Considering, however, the 0.6-eV energy separation between the two levels, our measured ratio is consistent with the population distribution characterized by an electron temperature in the discharge on the order of 1 eV. The relative number of atoms in the $1s_2$ and $1s_4$ resonance levels were measured by pumping the 826.3- and 805.9-nm transitions, respectively. A negligible fraction of atoms were found in these two $J=1$ resonance levels.

To determine the cross section for excitation out of a given metastable level individually, we modify the target composition by laser quenching. The Ti:sapphire laser is used to pump atoms out of one of the metastable levels into some higher level. Atoms excited into the higher level can decay back to the metastable level, or to resonance levels that decay to the ground state. With enough laser power, the metastable level being excited can be completely depopulated allowing us to extract unambiguous individual cross sections [7]. The quenching laser beam is positioned at the base of the hollow cathode discharge, before the atoms reach the electron-collision region. The Ti:sapphire laser is locked to the atomic transition of interest (monitored using the optogalvonic signal in a separate discharge) and a mechanical shutter is used to turn the quenching laser on/off. The excitation signal is recorded for the mixed target (laser off) and with the metastable level of interest removed (laser on). The difference in signal rates is due to excitation from that particular metastable level.

3. Relative calibration

The hollow cathode discharge apparatus was used to measure the excitation rates into all ten of the $4p^5 5p$ levels. To convert these relative signal rates into absolute cross sections, we ratio the results to the known $1s_5 \rightarrow 2p_9$ cross section measured with the fast beam apparatus (Sec. II A 3). The signal rate for a given emission line depends upon such factors as the metastable number density, the overlap of the electron and metastable beams, the solid angle of the detection optics, and the optical efficiency of the detection system at the wavelength of interest. Taking the ratio of two signal rates results in most of these factors dropping out, with the exception of the optical efficiency. To correct for the latter, we measure the desired transition signal from a Kr capillary-tube discharge lamp, $S_{\mathrm{lamp}}^{2p_x}$, for which the relative photon flux for each wavelength, $D_{\mathrm{lamp}}^{2p_x}$, was previously measured using a monochromator and a calibrated source of spectral irradiance. Combined with the branching fractions $\Gamma_\lambda^{2p_x}$ this yields cross sections from the equation

$$Q_m^{2p_x} = \frac{S_m^{2p_x}}{S_m^{2p_9}} \frac{\Gamma_\lambda^{2p_9}}{\Gamma_\lambda^{2p_x}} \frac{S_{\mathrm{lamp}}^{2p_9}}{S_{\mathrm{lamp}}^{2p_x}} \frac{D_{\mathrm{lamp}}^{2p_x}}{D_{\mathrm{lamp}}^{2p_9}} Q_m^{2p_9}, \qquad (9)$$

where $\Gamma_\lambda^{2p_9} = 1$, since the 811.3-nm wavelength transition is the only decay channel for this level. To obtain the branching

TABLE II. Apparent cross-section values from the $1s_5$ metastable level. Total uncertainties in the values are approximately ±35%, with the exception of the $2p_3$ and $2p_4$ levels where the uncertainty is approximately ±50%.

Energy	Cross section (10^{-16} cm^2)								
(eV)	$2p_2$	$2p_3$	$2p_4$	$2p_5$	$2p_6$	$2p_7$	$2p_8$	$2p_9$	$2p_{10}$
2	0	0	0	0.32	8.6	4.7	4.8	27	9.8
3	0.47	0.5	0.5	0.76	18	3.8	7.6	47	15
4	0.66	0.4	0.3	0.34	23	2.8	10	52	15
6	0.30	0.2	0.1	0.11	25	2.6	9.6	52	17
8	0.10	0.2	0.05	0.04	24	2.2	8.6	51	17
10					22		8.2	49	
15					17			41	
25					14			37	
50					8.8			23	
100					4.8			16	
200					3.1			8.9	
300					2.5			6.0	

fractions of the remaining levels we use the measurements of Dzierzega *et al.* [18].

Equation (9) only applies to excitation from the $1s_5$ metastable level. Since the $1s_3$:$1s_5$ number density ratio is approximately 1:12, for the same cross-section size, the signal rate for excitation from the $1s_3$ metastable level will be reduced by a factor of 12 relative to signal rate from the $1s_5$ metastable level. Hence for excitation from $1s_3$ metastable level Eq. (9) is modified by a factor of n_{1s_5}/n_{1s_3}. Measurement of this ratio is of special importance as it introduces an additional uncertainty in the cross sections out of the $1s_3$ beyond the ±35% uncertainty in the absolute calibration from the fast beam experiment, yielding a total systematic uncertainty on the order of ±40% for these cross sections.

III. RESULTS

As discussed in Sec. I, cross sections for core-preserving versus core-changing excitation processes are radically different. In organizing our results by these general groupings, we adopt the notation $2p$ (upper) and $2p$ (lower), respectively, for the upper ($2p_1$–$2p_4$) and lower ($2p_5$–$2p_{10}$) tiers of the $4p^5 5p$ configuration.

A. $1s_5 \rightarrow 2p$ (lower)

In Fig. 4 we plot the energy dependence of cross sections at low electron energies for core-preserving excitations from the $1s_5$ metastable level into the lower tier of $2p$. Our cross-section data are shown as discrete points with statistical error bars. Also included in the plots are five curves of theoretically calculated data which will be compared with our measurements in Sec. IV D. Numerical values of our measured cross sections at selected energies are listed in Table II. Although excitation from the $1s_5$ metastable level into levels with the same core can be broadly divided into being either

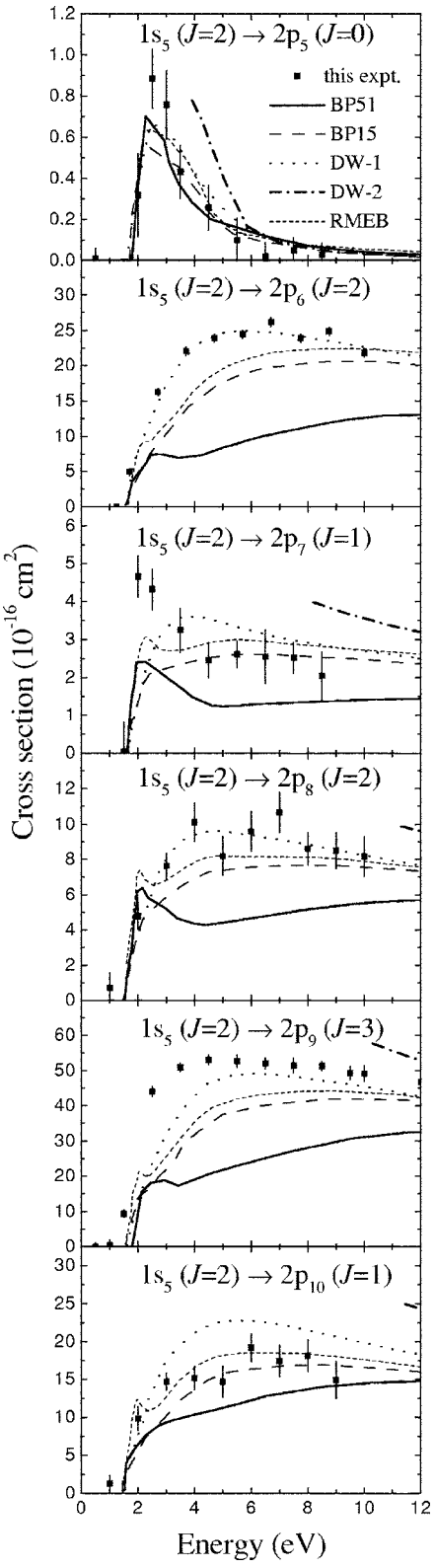

FIG. 4. Core-preserving cross sections for excitation into the lower tier levels (j_c=3/2) from the $1s_5$ level (j_c=3/2) as a function of the incident electron energy. Error bars are statistical only. Lines represent the different theoretical calculations from Ref. [8] (BP51, BP15, DW-1, DW-2) and the *R*-matrix calculation (RMEB) from Ref. [19].

dipole-allowed or dipole-forbidden, the results in Fig. 4 appear to fall into three categories. First, the cross section into the $2p_6$, $2p_8$, $2p_9$, and $2p_{10}$ levels are all generally large, characterized by a broad peak near 5 eV. Excitation into all of these levels are dipole-allowed from the $J=2$ $1s_5$ metastable level. For the second category we have the cross section for excitation into the $2p_5$ level which is much smaller than the other levels and has a sharp peak located very near threshold around 2.5 eV. Considering that excitation into the $J=0$ $2p_5$ level is dipole-forbidden from the $J=2$ $1s_5$ metastable level, this shape and small magnitude is consistent with our earlier findings for excitation from the metastable levels of Ar [4]. Intermediate between these two extremes is excitation into the $2p_7$ ($J=1$) level which is dipole-allowed but has a rather small dipole-matrix element in comparison with the first category. As a result, the magnitude of this cross section is smaller than the other dipole-allowed excitation processes. Note that the energy dependence for the $1s_5 \rightarrow 2p_7$ excitation cross section is also intermediate between the dipole-allowed and dipole-forbidden shapes (see Fig. 4). This point is discussed further in Sec. IV.

B. $1s_3 \rightarrow 2p$ (upper)

The energy dependence for the core-preserving excitation into the four $2p$ levels with $j_c=1/2$ are presented in Fig. 5 and the cross sections at selected energies in Table III. In contrast to the case of $1s_5 \rightarrow 2p$ (lower) we observe only two categories for this set of excitation cross sections. Excitation into the $J=1$ $2p_3$ and $2p_4$ levels is dipole-allowed from the $J=0$ $1s_3$ metastable level, and these cross sections are indeed very large with a broad peak at ~5 eV. For the two dipole-forbidden excitation processes, $1s_3 \rightarrow 2p_1$ ($\Delta J=0$, $0 \not\rightarrow 0$) and $1s_3 \rightarrow 2p_2$ ($\Delta J=2$), the cross sections are much smaller, with peaks near threshold. We find no intermediate category here since the oscillator strengths for the two dipole allowed transitions ($1s_3 \rightarrow 2p_3$, $1s_3 \rightarrow 2p_4$) are of comparable magnitude.

C. $1s_5 \rightarrow 2p$ (upper)

Cross-section results for three core-changing excitation processes from the $1s_5$ metastable level are shown in Fig. 6. All three of these excitation processes have very small cross sections with similar sharp peaks in the energy dependencies, even though all three excitations are dipole-allowed (cf. Sec. IV B). The signal rate for a particular $2p$ level measured with our mixed $1s_3$ and $1s_5$ target includes contributions from core-preserving excitation (large cross section) and core-changing excitation (small cross section). Since the signal rate is also dependent on the number densities of the $1s_5$ and $1s_3$ levels, the signal extraction process for determining core-changing cross sections into upper-tier $4p^5 5p$ levels is facilitated by the 12:1 ratio of $1s_5$:$1s_3$ metastable atoms in the unquenched target.

D. $1s_3 \rightarrow 2p$ (lower)

For populating the $2p$ levels in the lower tier in our experiment, the 12:1 ratio of $1s_5$:$1s_3$ number densities undesirably accentuates the core-preserving contribution out of the $1s_5$ levels, making it prohibitively difficult to extract the tiny core-changing contribution from the total excitation which is dominated by excitation out of the $1s_5$ metastable level. The only exception is the case of the $2p_7$ level because the core-preserving $1s_5 \rightarrow 2p_7$ cross section is relatively small, presenting the possibility of measuring the core-changing $1s_3 \rightarrow 2p_7$ cross section. Indeed, we observe a discernable change in the $2p_7$ excitation signal when we quench the $1s_3$ metastable level. Our data suggest that the peak $1s_3 \rightarrow 2p_7$ core-changing excitation cross section could be as large as 5×10^{-16} cm^2 but could also be much smaller because of the large experimental uncertainty. More accurate measurements are needed. If the $1s_3 \rightarrow 2p_7$ cross section should turn out to be close to the upper limit cited above, we would have an unexpected situation where the $1s_3 \rightarrow 2p_7$ core-changing cross section is similar in magnitude to its core-preserving counterpart $1s_5 \rightarrow 2p_7$.

E. High-energy results and the Born-Bethe approximation

Using the fast beam apparatus we have extended the measurements for the $1s_5 \rightarrow 2p_6$ and $1s_5 \rightarrow 2p_9$ cross sections to electron energies in excess of 300 eV (Fig. 7). At high electron energies, E, the dipole-allowed $i \rightarrow j$ excitation cross section is expected to vary according to the Born-Bethe approximation,

$$Q_{ij}^{BB}(E) \simeq 4\pi a_0^2 f_{ij} \frac{R^2}{E E_{ij}} \ln E, \tag{10}$$

where a_0 is the Bohr radius, R is the Rydberg energy, E_{ij} is the energy difference between the i and j energy levels, and f_{ij} is the oscillator strength of the $i \rightarrow j$ transition. In a plot of $Q \times E$ vs $\ln E$ one expects a straight line with a slope proportional to the optical oscillator strength. From our high-energy $1s_5 \rightarrow 2p_6$ and $1s_5 \rightarrow 2p_9$ cross-section results we obtain optical oscillator strengths of 0.28 ± 0.02 and 0.55 ± 0.05 (statistical uncertainties only). These agree very well with values derived spectroscopically of 0.24 and 0.50, respectively [18].

F. Cascade corrections

The apparent cross sections reported here are the sum of the direct excitation cross sections and the cascade contributions from excitation into higher levels that decay into the $4p^5 5p$ levels. As discussed in Sec. II A 3, one consequence of using the charge-exchange fast beam target is that the peak of the electron-impact excitation signal is shifted downstream along the direction of motion of atoms in the neutral beam by an amount proportional to the lifetime of the level of interest (see Fig. 3). The lifetime of the $2p_9$ level is 28 ns [20]. The shortest lifetime of a level that should contribute significantly to the cascades into the $2p_9$ level is 40 ns, with all other cascading levels having lifetimes in excess of 85 ns. If the cascade contribution from these long-lived levels to the $2p_9$ apparent cross section were significant, the experimental results in Fig. 3 would be shifted to larger separations between the electron beam and optical viewing region. Since the model Φ_f calculation fits the data very well without any

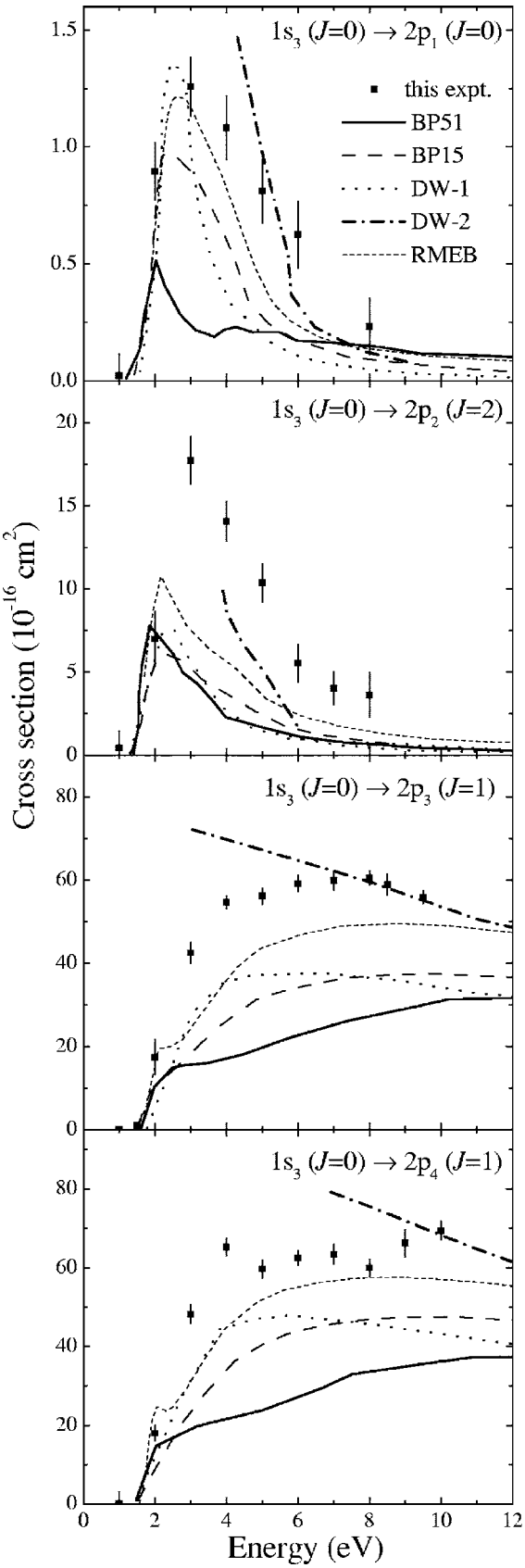

FIG. 5. Core-preserving cross sections for excitation into the upper tier levels (j_c=1/2) from the $1s_3$ level (j_c=1/2). Error bars are statistical only. Lines represent the theoretical calculations from Refs. [8,19].

TABLE III. Apparent cross-section values from the $1s_3$ metastable level. Total uncertainties in the values are approximately ±40%.

Energy	Cross section (10^{-16} cm^2)			
(eV)	$2p_1$	$2p_2$	$2p_3$	$2p_4$
2	0.90	7.0	17	18
3	1.3	18	43	48
4	1.1	14	55	65
6	0.63	5.5	59	62
8	0.23	3.6	60	63
10			56	67

long-lived contribution to the signal, we can rule out a significant cascade contribution to the $1s_5 \rightarrow 2p_9$ excitation cross section. A more quantitative analysis as in Ref. [12] yields conservative upper limits of 10% for the cascade contributions to both the $1s_5 \rightarrow 2p_6$ and $1s_5 \rightarrow 2p_9$ apparent cross sections. This 10% upper limit applies to the steady-state cascade contribution observed in a non-time-resolved experiment (such as the hollow cathode discharge experiment). For the fast beam target, this cascade contribution to the signal occurs predominantly at large separations between the electron beam and viewing region. The relative percentage of the cascade contribution to the observed signal is further reduced below 10% at small separations [12]. Nonetheless, the $1s_5 \rightarrow 2p_6$ and $1s_5 \rightarrow 2p_9$ apparent cross sections are two of the largest cross sections. Cascades may make up a larger percentage of the total apparent cross sections for the smaller cross sections reported here.

IV. DISCUSSION

A. Magnitude of cross sections

It is clear from the last section that those excitations conforming to both the optical dipole selection rules and the core propensity rule have the largest cross sections. As exemplified by the 6-eV values listed in the first section of Table IV (the first seven entries), the magnitude of these cross sections are seen to scale well with the optical oscillator strengths of the corresponding optical absorptions. Although the Born-Bethe approximation predicts this proportionality relation as given in Eq. (10), it is expected to hold only at high energies. Thus it is interesting to find the scaling relation valid even at an energy only four times the excitation threshold. To further explore this point we also include in Table IV the cross sections at 3.5 eV. Even at only twice the threshold energy there is still an excellent correlation with f_{ij} with the exception of the $1s_5 \rightarrow 2p_7$ excitation which has an anomalously small oscillator strength compared to the others in that group. For the $1s_5 \rightarrow 2p_7$ case the electron-excitation cross section is significantly larger than that expected from considering the oscillator strength alone. This deviation can be understood by comparing the energy dependence of the various cross sections shown in Figs. 4 and 5. With the exception of the $1s_5 \rightarrow 2p_7$ excitation, all of the other core-

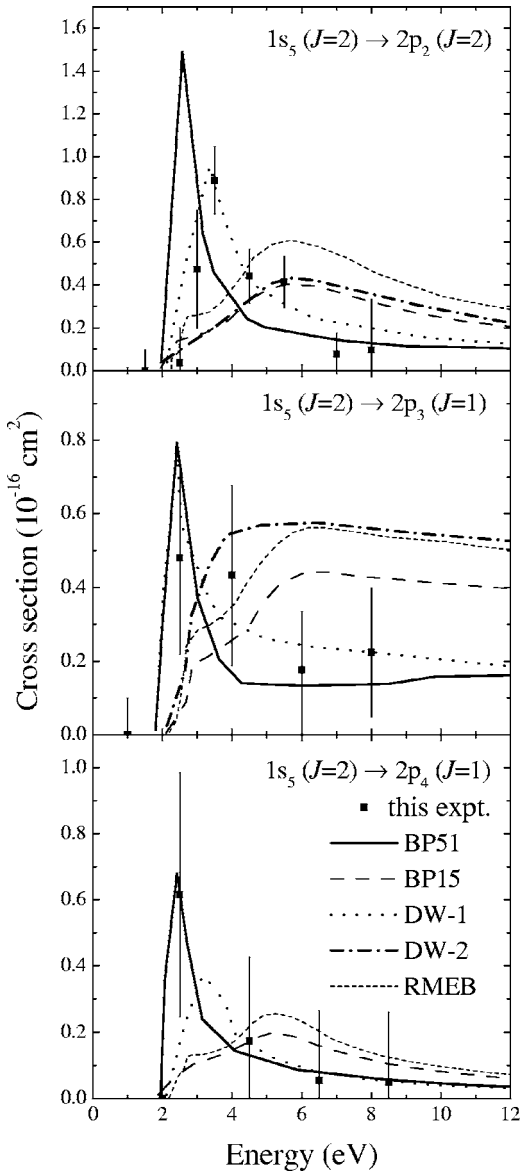

FIG. 6. Core-changing cross sections for excitation into the upper tier levels ($j_c=1/2$) from the $1s_5$ level ($j_c=3/2$). Error bars are statistical only. Lines represent the theoretical calculations from Refs. [8,19].

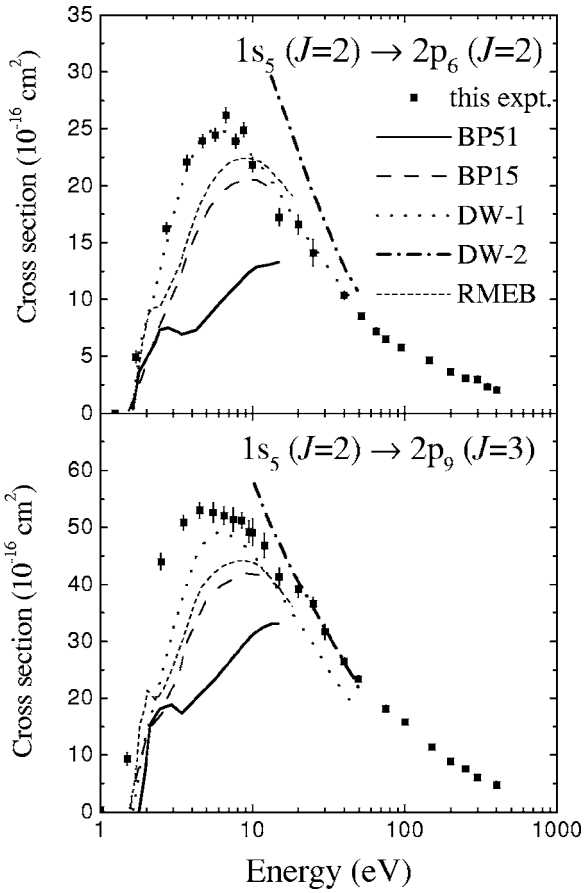

FIG. 7. High-energy cross sections results for excitation into the $2p_6$ and $2p_9$ levels from the $1s_5$ level. Error bars are statistical only. Lines represent the theoretical calculations from Refs. [8,19].

preserving, dipole-allowed excitation cross sections have a similar energy dependence. Hence if the cross sections track well with oscillator strength at one energy (i.e., 6 eV or higher), the similar shapes will ensure that the proportionality relation persists at energies down to the threshold energy. The $1s_5 \rightarrow 2p_7$ excitation, however, has a sharper peak than the other levels. Thus at low energies (i.e. 3.5 eV) the $1s_5 \rightarrow 2p_7$ cross section is larger than the value based on the relation with oscillator strength.

Since dipole-allowed, but core-changing excitation processes have small oscillator strengths, it is not surprising to find that these excitation processes also have very small cross sections. Here we find small peak cross sections of 0.9, 0.5, and 0.6×10^{-16} cm^2, for the $1s_5(J=2)\rightarrow 2p_2(J=2)$, $1s_5(J=2)\rightarrow 2p_3(J=1)$, and $1s_5(J=2)\rightarrow 2p_4(J=1)$ excitation processes, respectively. Comparison of cross sections at 3.5 and 6 eV with oscillator strengths for these excitations are listed in the middle section of Table IV (entries 8--10). Here the cross sections are mostly much larger than one would expect based solely on their oscillator strengths.

A third class of cross sections with intermediate values is formed by core-preserving excitations that are dipole forbidden. This class includes $1s_5(J=2)\rightarrow 2p_5(J=0)$, $1s_3(J=0) \rightarrow 2p_1(J=0)$, and $1s_3(J=0)\rightarrow 2p_2(J=2)$ with peak cross sections of 0.9, 1.3, and 17×10^{-16} cm^2, respectively. These cross sections are much smaller than those of core-preserving, dipole-allowed excitations out of the same initial level, but marginally larger than the core-changing cross sections. A more concrete comparison among these classes is to focus on excitation into the $2p_2(J=2)$ level where the core-preserving but dipole-forbidden excitation out of the $1s_3(J=0)$ overpowers the core-changing but dipole-allowed excitation out of the $1s_5(J=2)$.

B. Shape of excitation functions

In this section we discuss the criterion of dipole selection rules and core propensity in a more unified framework by considering the shape of the excitation functions. It is well known that the cross section for electron excitation corresponding to a dipole-allowed optical transition as a function

TABLE IV. Comparison of the measured $1s_y \rightarrow 2p_x$ cross sections (in 10^{-16} cm^2) at 3.5 and 6 eV with the corresponding optical oscillator strengths f_{ij} [18]. To aid in the comparison, in the fourth column we have multiplied f_{ij} by a normalization factor C chosen to match the $1s_5 \rightarrow 2p_9$ cross section. Error bars include both the statistical and systematic uncertainties.

Excitation $i \rightarrow j$	f_{ij}	Q (6 eV) (10^{-16} cm^2)	$f_{ij} \times C$ (scaled)	Q (3.5 eV) (10^{-16} cm^2)
$1s_3 \rightarrow 2p_3$	0.57	59±24	59	55±21
$1s_3 \rightarrow 2p_4$	0.46	62±25	48	64±25
$1s_5 \rightarrow 2p_6$	0.24	25±9	25	21±7
$1s_5 \rightarrow 2p_7$	0.023	2.6±0.9	2.4	3.2±1.1
$1s_5 \rightarrow 2p_8$	0.088	9.6±3.4	9.2	8.9±3.1
$1s_5 \rightarrow 2p_9$	0.50	52±18	(52)	52±18
$1s_5 \rightarrow 2p_{10}$	0.16	17±6	17	15±7
$1s_5 \rightarrow 2p_2$	5×10^{-4}	0.3±0.15	0.05	0.9±0.4
$1s_5 \rightarrow 2p_3$	0.003	0.2±0.1	0.28	0.5±0.3
$1s_5 \rightarrow 2p_4$	4×10^{-5}	0.1±0.05	0.004	0.4±0.2
$1s_3 \rightarrow 2p_1$	0	0.63±0.25	0	1.3±0.5
$1s_3 \rightarrow 2p_2$	0	5.5±2.2	0	16±6
$1s_5 \rightarrow 2p_5$	0	0.11±0.05	0	0.4±0.2

of electron energy has a broad maximum compared to non-dipole-type excitations for which the excitation functions have narrower peaks. For example, in the $1s_3 \rightarrow 2p$ (upper) data shown in Fig. 5 the two dipole-allowed excitations have broad peaks, ($1s_3 \rightarrow 2p_3$ and $1s_3 \rightarrow 2p_4$) whereas the two dipole-forbidden excitation processes have narrow peaks ($1s_3 \rightarrow 2p_1$ and $1s_3 \rightarrow 2p_2$). This is also mirrored in our measured excitation functions for the $1s_5 \rightarrow 2p$ (lower) series. Within this group the only non-dipole excitation is $1s_5 \rightarrow 2p_5$ which has a distinctly narrower peak in its excitation function than the other members (Fig. 4). As to the other five members, $1s_5 \rightarrow 2p_6$ through $1s_5 \rightarrow 2p_{10}$, that satisfy the dipole selection rules, the excitation functions all have a broad maximum except the $1s_5 \rightarrow 2p_7$ which has the smallest oscillator strength. Generally the cross section for each of the five excitations in this group, according to the Born-Bethe theory [i.e., Eq. (10)], consist of a leading term proportional to the optical oscillator strength. When the oscillator strength is of "normal" magnitude (i.e., >0.05), the leading term prevails resulting in a slow-varying energy dependence of the form $E^{-1}\ln E$. But if one member happens to have an unusually small oscillator strength (as in the case of $1s_5 \rightarrow 2p_7$), the "higher order" interactions beyond the leading dipole term (including exchange and indirect coupling) become more important and may cause a change of the shape of the excitation function.

The same consideration applies also to the core-changing excitations. All three excitation processes shown in Fig. 6 correspond to dipole-allowed transitions, so at first sight they could be candidates for broad-peak excitation functions. Experimentally this is clearly not the case as we can see in Fig. 6. This seeming anomaly is again traced to the exceptionally small oscillator strengths for the three cases (less than 0.01) on account of the core-changing nature.

The results enable us to study the systematics of dipole-allowed excitation out of a metastable level into the various levels within a configuration such as $4p^5 5p$ where the optical oscillator strength of each initial-to-final pair vary from 0.50 to 4×10^{-5}. An interesting finding is that the shape of the excitation function for the members of the $4p^5 5p$ configuration modulate accordingly. When the oscillator strength is above 0.05 we have the standard broad peak in the excitation function characteristic of dipole excitation. However, with decreasing oscillator strength the dipole-term in the cross section is reduced relative to the "higher order" terms referred to earlier and the gradual dominance of the latter manifests itself in a narrower peak. Such a continuous gradation from one extreme to another provides a unified view of the drastically different energy dependence of the cross sections observed for the core-preserving and core-changing excitation conforming to the dipole selection rules.

To fully appreciate the role of oscillator strength in determining the shape of dipole-allowed excitation functions we should contrast the present experiment for Kr($4p^5 5s \rightarrow 4p^5 5p$) excitation with electron-impact excitation from the ground state of He into the various n^1P levels. For the series of $(1s^2)^1S \rightarrow (1s)(np)^1P$ electron excitation with $n = 2, \ldots, 11$, the oscillator strength ranges from 0.276 to 0.0015 [21], yet measurements made in our laboratory yield excitation functions of the same broad-peak shape through $n=11$. Here we see no shape changes in the He $(1s)(np)^1P$ series because as we go up in n, the final-state charge cloud moves further away from the domain of the ground state so that the dipole term and the higher-order terms decrease together leaving the dominance of the dipole character intact. This distinguishes the He series from the case of Kr where we compare only levels within the $4p^5 5p$ configuration. In this connection we may point out a similar but much less extensive observation has been made for excitation from the $1s_5$ metastable level of Xe [22]. The excitation functions for Xe($1s_5 \rightarrow 2p_{6,8,10}$) (oscillator strengths of 0.24, 0.56, 0.24) all have a broad maximum whereas the Xe($1s_5 \rightarrow 2p_7$) (oscillator strength 0.015) curve shows a much narrower peak. Between these two limits we find an intermediate shape in the cross-section data for the Xe($1s_5 \rightarrow 2p_9$) which has an oscillator strength of 0.12.

C. Comparison to previous experiments

Excitation cross sections from the $1s_5$ metastable level to eight levels of the $4p^5 5p$ configuration have been previously measured by Mityureva, Penkin, and Smirnov [5]. In their experiment, a gas cell target ($\sim$100 mTorr) is excited by a dual electron beam pulse. The first high-energy pulse excites ground-state atoms into metastable levels, and a second, lower-energy, delayed pulse is used to excite the metastable atoms to higher energy levels. Absolute calibration is ob-

tained by combining the ratio of the fluorescence signals from the two pulses, a measurement of the fraction of metastable atoms in the target and the ground-state excitation cross section. They report very similar energy dependencies to those reported here; broad peaks for excitation from the $1s_5$ metastable level into the $2p_6$, $2p_8$, and $2p_9$ levels; narrower peaks for dipole-forbidden excitations ($2p_5$) and core-changing excitations ($2p_2$, $2p_3$, and $2p_4$). The magnitudes of their cross-section results, however, are between a factor of 10–20 times larger than our values. Since the ground-state excitation cross sections they used are generally within ±25% of the results of Ref. [11], the difference must lie in the measured Q_m/Q_{gs} ratio. Kolokolov and Terekhova [23] have used afterglow measurements in a He-Kr plasma to deduce rate coefficients and from these peak excitation cross sections for metastable excitation. The same energy dependence is assumed for all excitation processes. Their rate-coefficient analysis yields cross sections that are generally four to five times larger than our results.

D. Comparison to theoretical calculations

Hyman [24] applied the Born approximation to calculate the $4p^5 5s \rightarrow 4p^5 5p$ excitation cross sections but presented only configuration averaged cross sections. These averaged results can be weighted by the $1s_5 - 2p_x$ optical oscillator strengths to yield individual $1s_5 \rightarrow 2p_x$ cross sections. However, this precludes any comparison for dipole-forbidden excitations (i.e., $1s_5 \rightarrow 2p_5$) and necessarily assumes the same energy dependence for all dipole-allowed processes. A better comparison at low electron energies can be made with the recent calculations reported by Dasgupta *et al.* [8] and Zeng *et al.* [19]. In Ref. [8] the authors presented four sets of calculations which include two versions of the method of distorted waves (DW-1 and DW-2) and two calculations using the Breit-Pauli *R*-matrix method with 15 basis functions (BP15) and with 51 basis functions (BP51). The various approximations introduced in each set of calculations to make the computation tractable have been discussed in their earlier paper [25]. In Ref. [19] Zeng *et al.* have performed a relativistic *R*-matrix calculation with extended basis sets (RMEB). The theoretical values from both of these works are included in Figs. 4–6 for comparison with our experimental data. The DW-2 calculations tend to yield large cross sections at low energies and are not visible in some plots. At 10 eV the cross sections for a given excitation such as $1s_5 \rightarrow 2p_x$ calculated by the five methods usually range over a factor of 3. This reflects the difficulty of solving for the amplitude of electron inelastic scattering by a target atom with very complex excited-state electronic structure like Kr. Comparison between the theoretical and experimental cross sections should be useful in assessing the various methods of cross-section calculation and the approximations involved therein.

In discussing the experimental cross sections it should be kept in mind that while the absolute cross sections are subject to uncertainties in the range of 35–45%, the relative cross sections which are not affected by systematic errors have much higher precision of about 10% (i.e., the error bars in Fig. 5). Thus the analysis of the energy dependence of the cross section, in addition to the magnitude, is of special interest. The theoretical calculations of Refs. [8,19] fall into two general categories: the method of distorted waves and the method of close coupling (using the *R*-matrix technique). Thus comparison of the calculated cross sections with experiment will be discussed separately for these two methods.

For the large dipole-allowed, core-preserving excitation processes from the $1s_5$ metastable level (i.e., into the $2p_6$, $2p_8$, $2p_9$, and $2p_{10}$ levels) there is generally good agreement in both magnitude and energy dependence between our experimental results and the DW-1 calculations (see Fig. 4). The values from the DW-2 calculation, which are not unitarized, are generally too large making DW-1 the more preferred version at low energies; however, the DW-2 calculation does do a reasonable job at higher energies (see Fig. 7). The dipole-forbidden $1s_5 \rightarrow 2p_5$ excitation cross section also agrees very well in both magnitude and energy dependence with the DW-1 calculation. For the $1s_5 \rightarrow 2p_7$ dipole-allowed (but with a small dipole matrix element) excitation cross section, the DW-1 calculations agree fairly well with experiment above 4 eV, but do not reproduce the peak we observe at 2 eV. A comparable level of agreement exists between the DW-1 and the experimental results for the $1s_5$ core-changing cross sections displayed in Fig. 6. Finally we refer to Fig. 5 for core-preserving excitation out of the $1s_3$ metastable level. Although the DW-1 cross sections are smaller in magnitude than the experimental results, there is good agreement in the energy dependence. Considering the large (±40%) experimental uncertainties in the absolute cross sections out of the $1s_3$ metastable level, the overall level of agreement is fair.

As to the *R*-matrix close-coupling theory, results from the three sets of calculations are quite varied. The results of the two calculations using 15 basis functions (BP15) and 51 basis functions (BP51) reported in Ref. [8] differ quite significantly. In general the BP15 cross sections agree much better with experiment (to a level comparable to the DW-1 calculations). This is surprising since the BP51 calculation employs a larger basis set and should be closer to convergence. However, as explained in Ref. [25], BP15 and BP51 differ not only in the channels included but also in the target description. Nevertheless, one may be concerned about problems of convergence and the adequacy of the basis-function set. Ballance and Griffin recently have examined the issue of basis-set size and concluded that in their 235-level Breit-Pauli *R*-matrix–pseudostate calculation of Ne excitation cross sections, the pseudostate expansion is not sufficiently complete to represent the target continuum [26]. In their very recent *R*-matrix calculation of Kr excitation cross sections, Zeng *et al.* employed a very extended basis set and stated that they paid special attention to factors that may affect the convergence of the calculated cross sections. Their results, included in Figs. 4–7 as RMEB, are generally much closer to BP15 than to BP51. For core-preserving excitation from both the $1s_5$ and $1s_3$ metastable levels, the experimental cross sections are generally in good agreement with the RMEB and BP15 calculations, with the RMEB having better overall agreement in magnitude. For the $1s_5 \rightarrow 2p_7$ excitation cross section, while the RMEB calculation does have a small peak at 2 eV, only the BP51 curve reproduces the large peak at

2 eV observed experimentally; however, the magnitude of the BP51 calculation differs by a factor of 2 from the experimental results. Both the RMEB and BP51 calculations also yield a similar small peak at 2 eV for the $2p_8$ level that we do not observe. For the dipole-allowed, but core-changing excitations in Fig. 6 the BP51 calculation does the best job of reproducing the sharp peaks observed experimentally; both the BP15 and RMEB calculations indicate a broader peak at 6 eV which is absent in the BP51 curve. However, the unfavorable signal-to-noise ratio on these core-changing measurements makes a definitive comparison with theoretical calculations difficult. Some discussion about the differences and issue of convergence of the BP15 and BP51 calculations versus the RMEB work is found in Ref. [19].

E. Comparison with excitation from the ground state of Kr

One unique feature of excitation out of the metastable levels of Kr is the vast difference between excitation cross sections into the upper tier levels of the $4p^5 5p$ configuration ($j_c=1/2$) and those into the lower tier levels ($j_c=3/2$). The $1s_5 \rightarrow 2p$ (lower) excitations have order-of-magnitude larger cross sections than $1s_5 \rightarrow 2p$ (upper) group. Furthermore, the latter group exhibits a narrow excitation function even when the excitation corresponds to an optically allowed transition. In contrast for excitation out of the ground level into the $4p^5 5p$ configuration, such a sharp distinction between the upper and lower tier is not observed [11,14]. The peak cross sections for excitation from the ground level into the $2p_1 \cdots 2p_4$ are smaller than the cross sections into the $2p_5 \cdots 2p_{10}$ by only a factor of 2 (on the average) with no substantial differences in the general shape of excitation functions between the two groups [11]. The reason is that j_c is not a good quantum number for the closed-shell ground state of $(4p^6)\ ^1S_0$, thus the $\Delta j_c=0$ core propensity rule does not apply here. The electronic structure of the $4p^5 5s$ and $4p^5 5p$ excited configurations are strongly influenced by the coupling of the orbital and spin angular momentum vectors of the $4p^5$ ion core and of the $5s/5p$ outer electron, but the ground state is immune to the vector coupling scheme. The complexity of angular momentum coupling is felt in both the initial and final states for the $1s_5 \rightarrow 2p$ excitation, but only by the final state in the case of ground-state excitation.

Whereas the $4p^5 5s \rightarrow 4p^5 5p$ excitation is basically a dipole-type process with $\Delta l=1$ for the active electron, excitation from the $4p^6$ ground state into the $4p^5 5p$ levels (from $l=1$ into $l=1$) are of the monopolelike or quadrupolelike variety. Excitation from the ground state ($J=0$) into the $4p^5 5p$ levels with $J=0$ and $J=2$ are favored over those with $J=1$ and $J=3$. This is clearly evident in the size of the cross sections within each tier of the $4p^5 5p$ configuration at high energies and even generally valid at lower energies [11]. In contrast, excitation from the $1s_3$ metastable level favor only the $4p^5 5p$ levels with $J=1$, and excitation from the $1s_5$ metastable level favors levels with $J=1,2,3$ over those with $J=0$. Hence in a low-temperature plasma where excited levels can be populated by electron-impact excitation from atoms in both the ground state and the metastable levels, the ground-state excitation mechanism should dominate for $4p^5 5p$ levels with $J=0$, whereas the metastable stepwise excitation mechanism should be most important in populating the $4p^5 5p$ levels with $J=1$ and $J=3$ [27].

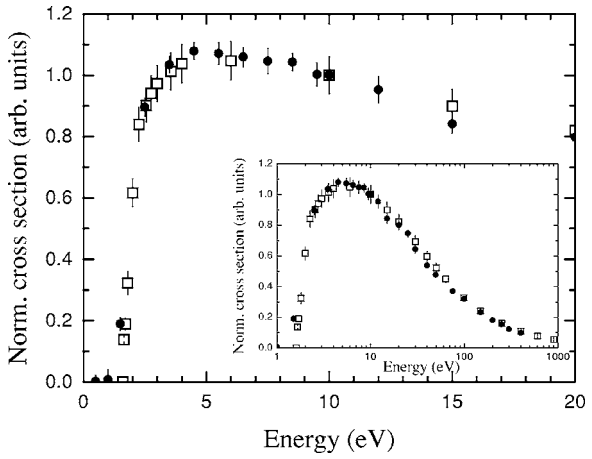

FIG. 8. Comparison of normalized excitation cross sections: ● $\mathrm{Kr}(1s_5 \rightarrow 2p_9)$ (this experiment), □ $\mathrm{Rb}(5S \rightarrow 5P)$ from Ref. [28]. Error bars are statistical only.

F. Comparison to excitation of alkali atoms

The ground state of the Rb atom has an electronic structure of $1s^2 \cdots 4p^6 5s$. Excitation of Rb from the $4p^6 5s$ ground state into the $4p^6 5p$ resonant level parallels the $\mathrm{Kr}(4p^5 5s \rightarrow 4p^5 5p)$ excitation except for the absence of an incomplete inner core thereby eliminating the complexity of angular momentum coupling in the initial and final states. The peak cross section for $\mathrm{Rb}(5S \rightarrow 5P)$ excitation is 67×10^{-16} cm^2 [28] comparable in magnitude to the sum of the peak cross sections for excitation from the $1s_5$ metastable level of Kr into all the $2p$ levels which is 100×10^{-16} cm^2. Even more remarkable is that the $\mathrm{Rb}(5S \rightarrow 5P)$ and $\mathrm{Kr}(1s_5 \rightarrow 2p_9)$ cross sections have identical energy dependence as shown in Fig. 8.

V. CONCLUSIONS

In studying electron-impact excitation out of the metastable levels of Kr we have examined 13 excitation processes $1s_3 \rightarrow 2p_x$ and $1s_5 \rightarrow 2p_x$ where the peak cross sections range from 0.5 to 50×10^{-16} cm^2 with a wide variety of energy dependencies. This wide spectrum of observed excitation behaviors provides a more comprehensive understanding of the collision dynamics especially from the standpoint of the electronic structure of the excited states involved. Take a rare-gas atom with ground state $(np)^6\ ^1S_0$ and consider excitation out of the metastable levels, $(np)^5(n+1)s$ with $J=0$ $(1s_3)$ and $J=2$ $(1s_5)$, into the ten $(np)^5(n+1)p$ levels with J ranging from 0 to 3. As far as the active electron is concerned, an analogy can be drawn to the $(n+1)s \rightarrow (n+1)p$ excitation in a quasi-one-electron atom which corresponds to a dipole excitation of generally large cross section and an excitation function with a broad maximum. However, the presence of the incomplete $(np)^5$ shell and its interactions

with the active electron alters the picture entirely. Each configuration of the type $(np)^5n'l$ consists of numerous levels characterized by the total angular momentum J. An excitation $(np)^5(n+1)s \rightarrow (np)^5(n+1)p$ with ΔJ that conforms to optical dipole selection rules have larger cross sections than a "dipole-forbidden" excitation. This general trend was observed in both Ar [4] and Ne [2].

Experiments on Kr reveal that beyond the dipole-forbidden or dipole-allowed cross section scaling relation that applies to the entire rare-gas series lies another core propensity rule that applies to Kr and Xe. The electronic structures of the $\mathrm{Kr}(4p^55s)$ and $\mathrm{Kr}(4p^55p)$ configurations differ from those of the corresponding configurations of $\mathrm{Ar}(3p^54s, 3p^54p)$ and $\mathrm{Ne}(2p^53s, 2p^53p)$ in one important aspect: the spin-orbit coupling of the $4p^5$ core is much larger than the coupling (via Coulomb and exchange) of the $4p^5$ core with the outer $5s/5p$ electron. This allows us to speak of the core angular momentum j_c which is approximately a good quantum number leading to the core propensity rule which strongly favors excitations with $\Delta j_c = 0$ over those with $\Delta j_c = \pm 1$. Thus the $\mathrm{Kr}(4p^55s \rightarrow 4p^55p)$ cross sections are gauged by not only the dipole selection rule which is common to all rare gases, but also the propensity rule which results from quantitative details of angular momentum coupling. In contrast, for Ar (or Ne) the spin-orbit coupling of the $3p^5$ core (or $2p^5$) is much weaker than the Coulomb interaction of the ion with the outer electron so that j_c is not a good quantum number—hence no propensity rule.

In this paper we examine the role of electronic structure and angular momentum coupling on the magnitude of excitation cross sections. Similar dependencies on the angular momentum values (J, j_c) have been found for coherence parameters describing the collisions between ground-state rare-gas atoms with spin-polarized electrons [29–31]. For example, the Stokes parameters, which describe the polarization of light emitted from the decay of $np^5(n+1)p$ levels, vary with the J value of the excited level [30]. In the case of Ne, experiments on $2p^6 \rightarrow 2p^53p$ $(J=1)$ excitation by spin-polarized electrons [31] indicate a larger polarization for levels with $j_c = 1/2$ than $j_c = 3/2$.

According to the Born-Bethe theory the cross section for electron excitation corresponding to an optically allowed transition is proportional to the absorption oscillator strength at high electron energies. Interestingly for excitation out of the metastable levels of Kr, this proportionality relation holds even down to energies as low as 3.5 eV except for very small oscillator strengths (i.e., less than 0.05) [7]. In that case the cross section is larger than expected from a direct proportionality relation and the peak in the excitation function is not as broad as those seen in the excitations corresponding to larger oscillator strengths. For electron-impact excitation out of the metastable levels of Kr into the $4p^55p$ manifold the oscillator strengths for the $1s_5 \rightarrow 2p_x$ and $1s_3 \rightarrow 2p_x$ series vary over a wide spectrum, from 0.57 down to less than 0.01. Echoing this variation is the shapes of dipole-allowed excitation functions which gradually change from the standard slow-varying $E^{-1}\ln E$ form into a sharp peak.

The rare-gas atoms afford an ideal opportunity to study the systematics of electron excitation. The cross sections for excitation into the ten levels of the $np^5n'p$ configuration show remarkable patterns of systematic variation with the J values of the initial and final levels. These patterns are common to the entire Ne-Ar-Kr-Xe sequence and are well explained by our multipole field model. In addition there are features that arise because of certain peculiarities of the electronic structure and the angular momentum coupling in the excited states of an individual atom (i.e., the large spin-orbit splittings of Kr-Xe). While Kr and Xe [22] both exhibit the core propensity rule, Kr is particularly interesting since the core-changing cross sections while small, are large enough to be easily measured. With the very large number of excited states with different modes of angular momentum coupling therein, studies of rare-gas excitation cross sections and their correlation with the electronic structure of the levels involved greatly enrich our understanding of electron excitation processes.

ACKNOWLEDGMENTS

The authors wish to thank T. Weber, Z. Staniszewski, and M. Gajda for work on some of the measurements. This work was supported by the National Science Foundation.

[1] J. O. Phelps and C. C. Lin, Phys. Rev. A **24**, 1299 (1981).
[2] J. B. Boffard, M. L. Keeler, G. A. Piech, L. W. Anderson, and C. C. Lin, Phys. Rev. A **64**, 032708 (2001).
[3] G. A. Piech, J. B. Boffard, M. F. Gehrke, L. W. Anderson, and C. C. Lin, Phys. Rev. Lett. **81**, 309 (1998).
[4] J. B. Boffard, G. A. Piech, M. F. Gehrke, L. W. Anderson, and C. C. Lin, Phys. Rev. A **59**, 2749 (1999).
[5] A. A. Mityureva, N. P. Penkin, and V. V. Smirnov, Opt. Spektrosk. **67**, 785 (1989) [Opt. Spectrosc. **67**, 461 (1989)].
[6] J. B. Boffard, T. E. Stone, L. W. Anderson, and C. C. Lin, Bull. Am. Phys. Soc. **46**, 9 (2001).
[7] R. O. Jung, T. E. Stone, J. B. Boffard, L. W. Anderson, and C. C. Lin, Phys. Rev. Lett. **94**, 163202 (2005).
[8] A. Dasgupta, K. Bartschat, D. Vaid, A. N. Grum-Grzhimailo, D. H. Madison, M. Blaha, and J. L. Giuliani, Phys. Rev. A **65**, 042724 (2002).
[9] J. B. Boffard, M. E. Lagus, L. W. Anderson, and C. C. Lin, Rev. Sci. Instrum. **67**, 2738 (1996).
[10] G. E. Ice and R. E. Olson, Phys. Rev. A **11**, 111 (1975).
[11] J. E. Chilton, M. D. Stewart, and C. C. Lin, Phys. Rev. A **62**, 032714 (2000).
[12] J. B. Boffard, M. F. Gehrke, M. E. Lagus, L. W. Anderson, and C. C. Lin, Eur. Phys. J. D **8**, 193 (2000).
[13] M. D. Stewart, J. E. Chilton, J. B. Boffard, and C. C. Lin, Phys. Rev. A **65**, 032704 (2002).
[14] S. Tsurubuchi, H. Kobayashi, and M. Hyodo, J. Phys. B **36**,

2629 (2003).
[15] J. E. Chilton, J. B. Boffard, R. S. Schappe, and C. C. Lin, Phys. Rev. A **57**, 267 (1998).
[16] S. Tsurubuchi, T. Miyazaki, and K. Motohashi, J. Phys. B **29**, 1785 (1996).
[17] R. B. Lockwood, L. W. Anderson, and C. C. Lin, Z. Phys. D: At., Mol. Clusters **24**, 155 (1992).
[18] K. Dzierzega, U. Volz, G. Nave, and U. Griesmann, Phys. Rev. A **62**, 022505 (2000).
[19] J. Zeng, J. Wu, F. Jin, G. Zhao, and J. Yuan, Phys. Rev. A **72**, 042707 (2005).
[20] NIST Atomic Spectra Database, URL http://physics.nist.gov/asd
[21] *Atomic Transition Probabilities*, Vol. I of Natl. Bur. Stand. (U.S.) Natl. Stand. Ref. Data. Series Circ. No. NSRDS-NBS 4, edited by W. L. Wiese, M. W. Smith, and B. M. Glennon (U.S. GPO, Washington D.C., 1966).
[22] R. O. Jung, J. B. Boffard, L. W. Anderson, and C. C. Lin, Phys. Rev. A **72**, 022723 (2005).
[23] N. B. Kolokolov and O. V. Terekhova, Opt. Spektrosk. **86**, 547 (1999) [Opt. Spectrosc. **86**, 481 (1999)].
[24] H. A. Hyman, Phys. Rev. A **18**, 441 (1978).
[25] A. Dasgupta, K. Bartschat, D. Vaid, A. N. Grum-Grzhimailo, D. H. Madison, M. Blaha, and J. L. Giuliani, Phys. Rev. A **64**, 052710 (2001).
[26] C. P. Ballance and D. C. Griffin, J. Phys. B **37**, 2943 (2004).
[27] C. C. Lin, Contrib. Plasma Phys. **44**, 405 (2004).
[28] S. T. Chen and A. C. Gallagher, Phys. Rev. A **17**, 551 (1978).
[29] D. H. Yu, P. A. Hayes, J. F. Williams, V. Zeman, and K. Bartschat, J. Phys. B **33**, 1881 (2000).
[30] V. Zeman, K. Bartschat, T. J. Gay, and K. W. Trantham, Phys. Rev. Lett. **79**, 1825 (1997).
[31] D. H. Yu, P. A. Hayes, J. F. Williams, and J. E. Furst, J. Phys. B **30**, 1799 (1997).